



Dust temperature in ALMA [C II]-detected high- z galaxies

L. Sommovigo,¹★ A. Ferrara,¹ S. Carniani^{1b},¹ A. Zanella,² A. Pallottini^{1b},¹ S. Gallerani¹ and L. Vallini^{1b}

¹*Scuola Normale Superiore, Piazza dei Cavalieri 7, I-56126 Pisa, Italy*

²*INAF – Osservatorio Astronomico di Padova, Vicolo Osservatorio 5, I-35122 Padova, Italy*

Accepted 2021 March 2. Received 2021 March 2; in original form 2020 November 30

ABSTRACT

At redshift $z > 5$, the far-infrared (FIR) continuum spectra of main-sequence galaxies are sparsely sampled, often with a single data point. The dust temperature $T_{\text{d,SED}}$, thus has to be assumed in the FIR continuum fitting. This introduces large uncertainties regarding the derived dust mass (M_{d}), FIR luminosity, and obscured fraction of the star formation rate. These are crucial quantities to quantify the effect of dust obscuration in high- z galaxies. To overcome observation limitations, we introduce a new method that combines dust continuum information with the overlying [C II] 158 μm line emission. By breaking the $M_{\text{d}}-T_{\text{d,SED}}$ degeneracy, with our method, we can reliably constrain the dust temperature with a single observation at 158 μm . This method can be applied to all Atacama Large Millimeter Array (ALMA) and NOEMA [C II] observations, and exploited in ALMA Large Programs such as ALPINE and REBELS targeting [C II] emitters at high- z . We also provide a physical interpretation of the empirical relation recently found between *molecular* gas mass and [C II] luminosity. We derive an analogous relation linking the *total* gas surface density and [C II] surface brightness. By combining the two, we predict the cosmic evolution of the surface density ratio $\Sigma_{\text{H}_2}/\Sigma_{\text{gas}}$. We find that $\Sigma_{\text{H}_2}/\Sigma_{\text{gas}}$ slowly increases with redshift, which is compatible with current observations at $0 < z < 4$.

Key words: methods: analytical – methods: data analysis – dust, extinction – galaxies: high-redshift – infrared: ISM.

1 INTRODUCTION

The *Hubble Space Telescope* (HST) and ground-based telescopes have been used to investigate the rest-frame ultraviolet (UV) emission from early galaxies (for a recent theoretical review, see Dayal & Ferrara 2018). The advent of high sensitivity millimetre interferometers such as the Atacama Large Millimeter Array (ALMA), allowed us for the first time to study also the far-infrared (FIR) emission from these sources (see e.g. Carilli & Walter 2013).

ALMA can detect both the FIR continuum and the brightest FIR lines in ‘normal’ (i.e. main sequence) galaxies at $z \geq 4$ (see e.g. Capak et al. 2015; Willott et al. 2015; Bouwens et al. 2016; Barisic et al. 2017; Carniani et al. 2017, 2018a, b; Laporte et al. 2017; Bowler et al. 2018; De Breuck et al. 2019; Tamura et al. 2019; Bakx et al. 2020; Béthermin et al. 2020; Schaerer et al. 2020). The FIR continuum is emitted as thermal radiation by dust grains, heated through the absorption of UV and optical light from newly born stars (see e.g. Draine 1989; Meurer, Heckman & Calzetti 1999; Calzetti et al. 2000; Weingartner & Draine 2001; Draine 2003).

The galaxy properties that mainly characterize the FIR continuum emission are the dust temperature $T_{\text{d,SED}}$ and the dust mass M_{d} , which are degenerate quantities. For the simultaneous determination of $T_{\text{d,SED}}$ and M_{d} , the most common approach is to fit the observed

spectral energy distribution (SED) with a single-temperature¹ grey-body function.

At $z \geq 5$ most of the sources observed with ALMA, when detected in dust continuum, have only a single (or very few) data point at FIR wavelengths (e.g. Bouwens et al. 2016; Barisic et al. 2017; Bowler et al. 2018; Hashimoto et al. 2019; Tamura et al. 2019). Consequently, $T_{\text{d,SED}}$ is assumed a priori in the fitting to reduce the degrees of freedom. The lack of knowledge of $T_{\text{d,SED}}$ results in very large uncertainties on the derived galaxy properties, such as M_{d} , the FIR luminosity L_{FIR} , and obscured star formation rate (SFR; for a detailed discussion, see e.g. Sommovigo et al. 2020). Further observations in a larger number of ALMA bands would ameliorate the problem, but not necessarily solve it. Indeed, mid-infrared (MIR) wavelengths remain inaccessible to ALMA. Nevertheless, the inclusion of ALMA band 7–8–9 data would improve the results significantly for galaxies at $z \gtrsim 5$. At these redshifts, these bands sample the SED at shorter wavelengths, closer to the FIR emission peak.

Here, we intend to overcome current observational limitations by combining dust continuum measurements with the widely observed fine-structure transition of singly ionized carbon [C II] at 158 μm . This line is the dominant coolant of the neutral atomic gas in the interstellar medium (Wolfire et al. 2003), making it one of the brightest FIR lines in most galaxies (Stacey et al. 1991). Moreover,

¹We underline that $T_{\text{d,SED}}$ does not necessarily correspond to the dust physical temperature, which is instead characterized by a probability distribution function (PDF; see e.g. Behrens et al. 2018; Sommovigo et al. 2020). In general, $T_{\text{d,SED}}$ does not necessarily provide a statistically sound representation of the PDF. For a discussion, see Appendix A.

★ E-mail: laura.sommovigo@sns.it

[C II] has been proved to be connected to the SFR of local (De Looze et al. 2014; Herrera-Camus et al. 2015) and high- z galaxies (see e.g. Capak et al. 2015; Maiolino et al. 2015; Pentericci et al. 2016; Carniani et al. 2017, 2018a, b, 2020; Matthee et al. 2017; Harikane et al. 2018; Smit et al. 2018).

In this work, we propose a novel method for the dust temperature computation using $L_{\text{C II}}$ as a proxy for the total gas mass, and therefore for M_d given a dust-to-gas ratio. Our method breaks the degeneracy between M_d and $T_{\text{d,SED}}$ in the SED fitting. This allows us to constrain $T_{\text{d,SED}}$ with a single continuum data point. As a byproduct of our method, we provide an interpretation of the empirical relation found by Zanella et al. (2018) between M_{H_2} and $L_{\text{C II}}$. We also derive a more general relation connecting the total gas mass M_{gas} with $L_{\text{C II}}$. Joining the two, we can also study the evolution of the molecular gas fraction $M_{\text{gas}}/M_{\text{H}_2}$ with redshift.

The paper² is organized as follows. We present our method for the dust temperature derivation in Section 2, and we test it on a sample of local galaxies (Section 3). We then apply the method to the few high- z galaxies ($z > 4$; Section 4) for which multiple FIR continuum observations are available in the literature. In Section 5, we discuss additional outputs, i.e. the physical explanation for the relation by Zanella et al. (2018), and the molecular gas fraction evolution with z . In Section 6, we summarize our results and discuss future applications.

2 METHOD

Before introducing our method, we discuss two key ingredients, i.e. the dust-to-gas ratio D and the conversion factor $\alpha_{\text{C II}} = M_{\text{gas}}/L_{\text{C II}}$. Multiplying $L_{\text{C II}}$ by the product $D \cdot \alpha_{\text{C II}}$ we infer M_d . We can then constrain $T_{\text{d,SED}}$ using a single continuum data point.

2.1 Dust-to-gas ratio

Several studies (e.g. James et al. 2002; Draine & Li 2007; Galliano, Dwek & Charnal 2008; Leroy et al. 2011) have shown that D scales linearly with metallicity, with little scatter, down to $Z \lesssim 0.1 Z_\odot$:

$$D = D_{\text{MW}} \left(\frac{Z}{Z_\odot} \right), \quad (1)$$

where $D_{\text{MW}} = 1/162$ is the Milky Way dust-to-gas ratio (Rémy-Ruyer et al. 2014). We adopt equation (1) as our fiducial choice, since almost all the galaxies to which we apply our method have metallicities $\gtrsim 0.2 Z_\odot$. Hence, they are mostly unaffected by deviations³ from this linear scaling that might occur at $Z \lesssim 0.1 Z_\odot$.

Moreover, the ideal targets of our method are the galaxies observed in current high- z ALMA surveys (such as e.g. ALPINE, PI: Le Fèvre, and REBELS, PI: Bouwens), which are massive (stellar mass $M_\star \simeq 10^{10} M_\odot$), dusty, and evolved sources. From numerical simulations,

galaxies at $z \sim 6$ with similar stellar masses ($10^9 < M_\star < 10^{11}$) are expected to have $Z \gtrsim 0.1 Z_\odot$ (Ma et al. 2016; Torrey et al. 2019). This is also confirmed, albeit with considerable uncertainties (relative errors up to ~ 80 per cent), by several studies that analyse FIR line (such as [N II], [N III], [C II], C III], and [O III]) observations at $z \gtrsim 6$ –8 to derive Z (see e.g. Pereira-Santaella et al. 2017; De Breuck et al. 2019; Hashimoto et al. 2019; Tamura et al. 2019; Bakx et al. 2020; Jones et al. 2020; Vallini et al. 2020, and references therein).

Current estimates of Z at high redshift will be significantly ameliorated thanks to forthcoming ALMA observations and to the *James Web Space Telescope* (JWST) spectroscopy. Indeed, JWST will detect several optical nebular lines (such as H β , H α , [N II], [O II], and [O III]) out to $z \sim 10$. This will allow us to reduce the relative errors associated with Z down to ~ 35 per cent even at very high- z (see e.g. Wright et al. 2010; Chevallard et al. 2019; Maiolino & Mannucci 2019), improving also our knowledge of the dust-to-gas ratios.

2.2 [C II]-to-total gas mass conversion factor

The [C II] conversion factor, $\alpha_{\text{C II}}$, expresses the specific [C II] emission efficiency per unit total (i.e. atomic + molecular) gas mass. To investigate the relation between total $L_{\text{C II}}$ and M_{gas} , we use the following empirical relations:⁴

$$\Sigma_{\text{SFR}} = 10^{-6.99} \Sigma_{\text{C II}}^{0.93} \quad (\text{De Looze relation}), \quad (2)$$

$$\Sigma_{\text{SFR}} = 10^{-12} \kappa_s \Sigma_{\text{gas}}^{1.4} \quad (\text{Kennicutt–Schmidt relation}), \quad (3)$$

$$\Sigma_{\text{gas}} = \alpha_{\text{C II}} \Sigma_{\text{C II}} \quad (\text{conversion relation}). \quad (4)$$

The first relation has been inferred by De Looze et al. (2014, hereafter DL) from the Dwarf Galaxy Survey (DGS) sample of local galaxies.⁵ The second one is the Kennicutt–Schmidt relation (Kennicutt et al. 1998, hereafter KS). The ‘burstiness parameter’ κ_s quantifies the single source deviations (upwards for starbursts, and downwards for quiescent galaxies; see Heiderman et al. 2010; Ferrara et al. 2019) from the average relation. Finally, equation (4) is equivalent to the definition $\alpha_{\text{C II}} = M_{\text{gas}}/L_{\text{C II}}$ under the assumption that [C II] is spatially extended as the gas.

We combine equations (2)–(4) into the following one:

$$\alpha_{\text{C II}} = \frac{11.3}{\kappa_s^{5/7}} \Sigma_{\text{SFR}}^{-0.36} \frac{M_\odot}{L_\odot}. \quad (5)$$

This relation shows that satisfying the DL and KS relations at the same time implies that $\alpha_{\text{C II}}$ cannot be constant. It must depend on the SFR and its mode (burst versus quiescent). At a fixed SFR, galaxies with large κ_s values (starbursts) have a lower $\alpha_{\text{C II}}$ and therefore can produce a larger [C II] luminosity per unit gas mass. The same is true if κ_s is fixed and the SFR is larger. In high star formation regimes, the more efficient [C II] emission might depend on a more intense radiation field or higher gas density (Ferrara et al. 2019; Pallottini et al. 2019).

2.2.1 Modification at high- z

As we approach the Epoch of Reionization (EoR), a precise assessment of the KS relation becomes very difficult. H I is not observable

²Throughout the paper, we assume a flat Universe with the following cosmological parameters: $\Omega_m h^2 = 0.1428$, $\Omega_\Lambda = 1 - \Omega_m$, and $\Omega_b h^2 = 0.02233$, $h = 67.32$, $\sigma_8 = 0.8101$, where Ω_m , Ω_Λ , and Ω_b are the total matter, vacuum, and baryonic densities, respectively, in units of the critical density; h is the Hubble constant in units of 100 km s^{-1} , and σ_8 is the late-time fluctuation amplitude parameter (Planck Collaboration VI 2018).

³At very low metallicities ($Z \lesssim 0.1 Z_\odot$), deviations from the linear relation have been suggested (see e.g. Galliano et al. 2005; Galametz et al. 2011; Rémy-Ruyer et al. 2014; De Vis et al. 2019). For instance, Rémy-Ruyer et al. (2014) find a steeper D – Z relation in their sample of local galaxies. However, the deviation is driven especially by the fewer, widely scattered data at $Z \leq 0.1 Z_\odot$.

⁴We adopt the standard units used for these quantities: surface star formation [$M_\odot \text{ kpc}^{-2} \text{ yr}^{-1}$], [C II] luminosity [$L_\odot \text{ kpc}^{-2}$], and gas density [$M_\odot \text{ kpc}^{-2}$].

⁵For details on the DGS sample, see Section 3.

at $z \geq 4$, and typical H_2 tracers (CO and dust) suffer from severe limitations.⁶ Hence, Σ_{gas} is not reliably measurable. So far there is considerable evidence that FIR-detected galaxies at $z > 5$ are strong UV emitters⁷ with large SFRs, i.e. they are most likely starbursts ($\kappa_s \gg 1$; see e.g. Vallini et al. 2020; Vallini, in preparation).

The validity of the DL relation might also be questioned at high- z . Most studies agree that this relation is still valid at $z > 4$, although its scatter is ~ 2 times larger than the local one (Carniani et al. 2018a, b; Matthee et al. 2019; Schaerer et al. 2020). However, in extreme cases (SFR $< 30\text{--}50 M_\odot \text{ yr}^{-1}$ or $z > 8$) high- z sources have been found to deviate more than 2σ from the local DL relation, being systematically below the latter (Knudsen et al. 2016; Pentericci et al. 2016; Bradač et al. 2017; Laporte et al. 2019; Matthee et al. 2019).

Recently, Carniani et al. (2020) showed that EoR galaxies lay on the slightly different (w.r.t. the one in equation 2) DL relation appropriate for starburst/H II-like galaxies⁸

$$\Sigma_{\text{SFR}} = 10^{-7.06} y^2 \Sigma_{\text{CII}} \quad (\text{DeLooze relation/starbursts}), \quad (6)$$

once that obscured fraction of the SFR is appropriately included in Σ_{SFR} . The factor $y = r_{\text{CII}}/r_*$ is introduced since there is growing evidence that at $z > 4$ [C II] emission is more extended than UV emission ($1.5 \lesssim y \lesssim 3$ at $z > 4$; see e.g. Carniani et al. 2017, 2018a, 2020; Matthee et al. 2017, 2019; Fujimoto et al. 2019, 2020; Ginolfi et al. 2020). The origin of such extended [C II] structure is still debated. Current explanations range from emission by (i) outflow remnants in the circumgalactic medium (CGM; see e.g. Maiolino et al. 2015; Vallini et al. 2015; Gallerani et al. 2017; Fujimoto et al. 2019; Ginolfi et al. 2020; Pizzati et al. 2020), (ii) CGM gas illuminated by the galaxies strong radiation field (Carniani et al. 2017, 2018b; Fujimoto et al. 2020), to (iii) actively accreting satellites (Pallottini et al. 2017a; Carniani et al. 2018a; Matthee et al. 2019).

By combining equation (6) with equations (3) and (4), we derive the high- z conversion factor

$$\alpha_{\text{CII,hz}} = \frac{32.47}{\kappa_s^{5/7}} y^2 \Sigma_{\text{SFR}}^{-0.29} \frac{M_\odot}{L_\odot}. \quad (7)$$

Using the DL relation for starbursts, independently on the chosen factor y , results in a rescaling upwards of α_{CII} at high- z with respect to $z \simeq 0$. The dependence on Σ_{SFR} and κ_s is almost unchanged. Additionally, at a fixed SFR and κ_s , galaxies with lower y (less extended [C II] emission) have a lower α_{CII} , i.e. a larger [C II] luminosity per unit gas mass.

2.3 Dust temperature

We assume an optically thin, single-temperature, grey-body approximation. The dust continuum flux F_ν observed against the CMB at

⁶Observing CO transitions becomes challenging due to the larger cosmological distance of sources, and lower contrast against the cosmic microwave background (CMB; see e.g. da Cunha et al. 2013). This also makes dust emission observations more difficult at high- z . This is particularly true in the presence of cold dust nearly in equilibrium with the CMB (da Cunha et al. 2013). Most importantly, the impossibility to simultaneously constrain M_d and $T_{\text{d,SED}}$ due to the few available data points, results in very large uncertainties on M_d , and therefore M_{H_2} .

⁷This might, however, be due to an observational bias. Indeed, most high- z ALMA targets have been selected from UV observations (i.e. by construction they are strong UV emitters). There are few exceptions represented by the (sub)mm-selected targets, as in the surveys ASPECS (Walter et al. 2016) and SPT (Weiß et al. 2013).

⁸That is also provided in DL.

rest-frame frequency ν can be written as (see e.g. da Cunha et al. 2013; Kohandel et al. 2019)

$$F_\nu = g(z) M_d \kappa_\nu [B_\nu(T'_{\text{d,SED}}) - B_\nu(T_{\text{CMB}})], \quad (8)$$

where $g(z) = (1+z)/d_L^2$, d_L is the luminosity distance to redshift z , κ_ν is the dust opacity, B_ν is the blackbody spectrum, and $T_{\text{CMB}}(z)$ is the CMB temperature⁹ at redshift z .

At wavelengths $\lambda > 20 \mu\text{m}$, κ_ν can be approximated as (Draine 2004)

$$\kappa_\nu = \kappa_* \left(\frac{\nu}{\nu_*} \right)^\beta, \quad (9)$$

where the choice of (κ_*, ν_*, β) depends on the assumed dust properties. We consider Milky Way-like dust, for which standard values are $(\kappa_*, \nu_*, \beta) = (52.2 \text{ cm}^2 \text{ g}^{-1}, 2998 \text{ GHz}, 2)$ (see Dayal, Hirashita & Ferrara 2010). We also account for the fact that the CMB acts as a thermal bath for dust grains, setting a lower limit for their temperature. We correct $T_{\text{d,SED}}$ for this effect, following the prescription¹⁰ by da Cunha et al. (2013).

Equation (8) has two parameters, M_d and $T_{\text{d,SED}}$. [C II] observations can be used to determine M_d :

$$M_d = D M_{\text{gas}} = D \alpha_{\text{CII}} L_{\text{CII}}. \quad (10)$$

We substitute in equation (8) and specialize to the [C II] line frequency $\nu_0 = 1900.54 \text{ GHz}$. We thus introduce the [C II]-based dust temperature $T_{\text{d,CII}}$, defined as the solution of

$$F_{\nu_0} = g(z) D \alpha_{\text{CII}} L_{\text{CII}} \kappa_{\nu_0} [B_{\nu_0}(T_{\text{d,CII}}) - B_{\nu_0}(T_{\text{CMB}})]. \quad (11)$$

We can rewrite this equation in a more compact form, yielding the explicit expression for $T_{\text{d,CII}}$:

$$T_{\text{d,CII}} = \frac{T_0}{\ln(1 + f^{-1})}, \quad (12)$$

where $T_0 = h_P \nu_0 / k_B = 91.86 \text{ K}$ is the temperature corresponding to the [C II] transition energy (k_B and h_P are the Boltzmann and Planck constants). We have defined:

$$f = \mathcal{B}(T_{\text{CMB}}) + A^{-1} \tilde{F}_{\nu_0}, \quad (13)$$

where $\mathcal{B}(T_{\text{CMB}}) = [\exp(T_0/T_{\text{CMB}}) - 1]^{-1}$. The non-dimensional continuum flux \tilde{F}_{ν_0} and the constant A are defined as

$$\begin{aligned} \tilde{F}_{\nu_0} &= \frac{\lambda_0^2 F_{\nu_0}}{2 k_B T_0} = 0.98 \times 10^{-16} \left(\frac{F_{\nu_0}}{\text{mJy}} \right), \\ A &= g(z) \alpha_{\text{CII}} D L_{\text{CII}} k_0 \\ &= 5.2 \times 10^{-24} \left[\frac{g(z)}{g(6)} \right] \left(\frac{L_{\text{CII}}}{L_\odot} \right) \left(\frac{\alpha_{\text{CII}}}{M_\odot/L_\odot} \right) D. \end{aligned} \quad (14)$$

Clearly, if $\tilde{F}_{\nu_0}/A \gg \mathcal{B}(T_{\text{CMB}})$ the CMB effects on dust temperature become negligible.

Equation (12) can be used to compute T_{CII} using a single 1900 GHz observation (which provides both L_{CII} and F_{ν_0}) once one has an estimate for the two parameters D (Section 2.1) and α_{CII} (Section 2.2).

2.3.1 Numerical implementation

Writing explicitly the expressions for D and α_{CII} in equation (14), we can show that $T_{\text{d,CII}}$ is ultimately a function of the following

⁹ $T_{\text{CMB}}(z) = T_{\text{CMB},0}(1+z)$, with $T_{\text{CMB},0} = 2.7255 \text{ K}$ (Fixsen 2009).

¹⁰ $T'_{\text{d,SED}} = \{T_{\text{d,SED}}^{4+\beta} + T_{\text{CMB},0}^{4+\beta} [(1+z)^{4+\beta} - 1]\}^{1/(4+\beta)}$. In the following, we drop the apex from the dust temperature symbol for better readability. It is then intended we always refer to the CMB-corrected dust temperature.

Table 1. Properties of galaxies included in our benchmark local sample. For the data without specified uncertainty, we consider a 20 per cent relative error as a conservative choice.

ID	Galaxy	ν_2 (GHz)	F_{ν_2} (Jy)	d_L (Mpc)	F_{ν_0} (Jy)	Z (Z_\odot)	$\log \Sigma_{\text{SFR}}$ ($\text{M}_\odot \text{ yr}^{-1} \text{ kpc}^{-2}$)	$\log L_{\text{C II}}$ (L_\odot)	κ_s	$T_{\text{d,SED}}$ (K)	$T_{\text{d,C II}}$ (K)
0	UGC4483 ^a	4285	0.109 ± 0.007	3.2	0.081 ± 0.029	0.053	-3.041	4.119	0.1	$31.0^{+5.0}_{-2.0}$	$32.0^{+7.0}_{-7.0}$
1	VIIZw403 ^a	4285	0.493 ± 0.026	4.5	0.260 ± 0.037	0.083	-2.621	4.994	0.3	$34.0^{+2.0}_{-1.0}$	$30.0^{+4.0}_{-6.0}$
2	NGC 1569 ^a	4285	42.600 ± 2.100	3.1	39.700 ± 4.800	0.190	-1.721	6.669	3.1	$29.0^{+1.0}_{-1.0}$	$34.0^{+5.0}_{-7.0}$
3	II Zw 40 ^a	4285	5.580 ± 0.280	12.1	3.140 ± 0.431	0.309	-0.818	6.586	0.9	$33.0^{+2.0}_{-1.0}$	$43.0^{+7.0}_{-11.0}$
4	NGC 4214 ^a	4285	20.400 ± 1.020	2.9	23.400 ± 2.820	0.331	-3.054	5.977	0.4	$28.0^{+1.0}_{-1.0}$	$27.0^{+3.0}_{-5.0}$
5	UM 448 ^a	4285	4.040 ± 0.203	87.8	2.850 ± 0.345	0.380	-0.957	8.281	0.8	$31.0^{+1.0}_{-1.0}$	$37.0^{+6.0}_{-8.0}$
6	NGC 1140 ^a	4285	3.430 ± 0.172	20	4.050 ± 0.487	0.436	-2.096	7.169	0.1	$27.0^{+1.0}_{-1.0}$	$26.0^{+3.0}_{-5.0}$
7	LARS2 ^b	4285	0.080 ± 0.011	131.4	0.121 ± 0.014	0.309	-2.901	7.230	0.1	$26.0^{+1.0}_{-1.0}$	$24.0^{+7.0}_{-5.0}$
8	LARS3 ^b	4285	9.306 ± 0.008	138.7	4.745 ± 0.019	0.468	-1.444	9.190	2.7	$34.0^{+1.0}_{-1.0}$	$24.0^{+4.0}_{-4.0}$
9	LARS8 ^b	2998	4.322 ± 0.027	169.6	3.346 ± 0.034	0.589	-1.850	9.550	1.1	$24.0^{+2.0}_{-2.0}$	$18.0^{+2.0}_{-2.0}$
10	LARS9 ^b	4285	1.147 ± 0.017	208.7	1.306 ± 0.027	0.427	-0.425	9.170	0.3	$25.0^{+2.0}_{-2.0}$	$28.0^{+5.0}_{-6.0}$
11	LARS12 ^b	4285	0.104 ± 0.004	473.8	0.062 ± 0.004	0.398	-2.021	8.580	5.1	$33.0^{+1.0}_{-1.0}$	$20.0^{+3.0}_{-3.0}$
12	LARS13 ^b	4283	0.506 ± 0.003	701.1	0.286 ± 0.003	0.575	-1.333	9.250	4.5	$33.0^{+1.0}_{-1.0}$	$25.0^{+4.0}_{-5.0}$
13	NGC 4631 ^c	3409	31.11	6.2	34.23	0.50	-3.18	6.91	0.4	$24.0^{+3.0}_{-2.0}$	$22.0^{+3.0}_{-3.0}$
14	NGC 3627 ^c	3409	20.68	9.3	17.40	1.77	-2.85	6.46	0.7	$27.0^{+3.0}_{-3.0}$	$23.0^{+3.0}_{-4.0}$
15	NGC 2146 ^c	3409	137.93	12.9	229.17	0.98	-2.03	8.28	0.1	$21.0^{+2.0}_{-2.0}$	$25.0^{+4.0}_{-5.0}$
16	NGC 3938 ^c	3409	30.41	17.9	38.72	2.10	-2.98	6.80	0.1	$23.0^{+2.0}_{-2.0}$	$31.0^{+6.0}_{-7.0}$
17	M83 ^c	3409	135.78	7.4	111.93	1.23	-2.87	7.37	0.5	$27.0^{+4.0}_{-3.0}$	$21.0^{+3.0}_{-3.0}$
18	M82 ^c	3409	1117.00	2.9	614.57	2.75	-1.56	7.38	5.9	$32.0^{+5.0}_{-4.0}$	$21.0^{+3.0}_{-3.0}$

^aNilson (1973); Engelbracht et al. (2008); DL; Cormier et al. (2019).^bPuschnig et al. (2020).^cJarrett et al. (2003); Caldú-Primo & Cruz-González (2008); Leroy et al. (2008); Groves et al. (2015); Fernandez-Ontiveros et al. (2016).

parameters (κ_s , z , F_{ν_0} , Z , Σ_{SFR} , $L_{\text{C II}}$). For local galaxies, all these quantities are well constrained by observations. In practice, we solve equation (12) performing a random sampling of these parameters around the measured values, within the uncertainties. Differently, at high- z κ_s is largely unknown.¹¹ Hence, we consider a broad random uniform distribution for this parameter.

To constrain $T_{\text{d,C II}}$ at high- z , we add the following physical conditions:

(i) M_d does not exceed the largest dust mass producible by supernovae (SNe), $M_{\text{d,max}}$. To quantify $M_{\text{d,max}}$, we take a metal yield constraint $y_Z < 2 \text{ M}_\odot$ per SN, and assume that all the produced metals are later included in dust grains. Then:

$$M_{\text{d,max}} = y_Z \nu_{\text{SN}} M_\star, \quad (15)$$

where $\nu_{\text{SN}} = (53 \text{ M}_\odot)^{-1}$ is the number of SNe per solar mass of stars formed for a standard Salpeter 1–100 M_\odot initial mass function (Ferrara & Tolstoy 2000).

(ii) $\text{SFR}_{\text{FIR}} \sim 10^{-10} L_{\text{FIR}}$ (KS), does not exceed the total measured SFR. This directly relates to the dust mass and temperature as $L_{\text{FIR}} = M_d (T_{\text{d,C II}}/6.73)^6$ (Dayal et al. 2010).

$T_{\text{d,C II}}$ solutions not satisfying (i) and (ii) are discarded. These conditions result in a lower (upper) cut for very cold (hot) dust temperatures corresponding to unphysically large dust masses (FIR luminosity and SFR). This allows us to effectively constrain $T_{\text{d,C II}}$ at high- z despite the lack of information on κ_s .

3 LOCAL TESTING

We have selected 19 local galaxies for which the needed data are available: (i) κ_s , (ii) redshift, (iii) metallicity, (iv) total SFR and Σ_{SFR} , (v) total $L_{\text{C II}}$, and (vi) at least two FIR continuum detections, one of which is at ν_0 . These galaxies are drawn from the following catalogues:¹²

(i) DGS (see e.g. DL; Madden et al. 2014, 2020): targeting a total of 50 local dwarf galaxies, whose [C II], [O I], and [O III] line emissions are mapped with the *Herschel Space Observatory*.

(ii) Lyman Alpha Reference Sample (LARS; see e.g. Hayes et al. 2014; Östlin et al. 2014): consisting of 14 low-redshift ($z = 0.03$ – 0.2) mildly starbursting systems observed in multiple bands with *HST*. This sample was intended as a local laboratory for the study of Ly α , which is one of the dominant lines used to characterize high- z sources;

(iii) The complete data base of the Herschel/Photoconductor Array Camera and Spectrometer (PACS; see Fernandez-Ontiveros et al. 2016): a coherent data base of spectroscopic observations of FIR fine-structure lines (in the range 10–600 μm) collected from the Herschel/PACS spectrometer archive for a local sample of 170 active galactic nuclei (AGNs), 20 starburst, and 43 dwarf galaxies.

The selected galaxies and their properties are reported in Table 1. Hereafter, we refer to these galaxies as the *local sample*.

¹¹At high- z , we also introduce the parameter y . This is often well constrained by observations.

¹²Other local samples, such as KINGFISH (Kennicutt et al. 2011) and GOALS surveys (Chu et al. 2017), lack one of the required data (total [C II] luminosity and metallicity, respectively).

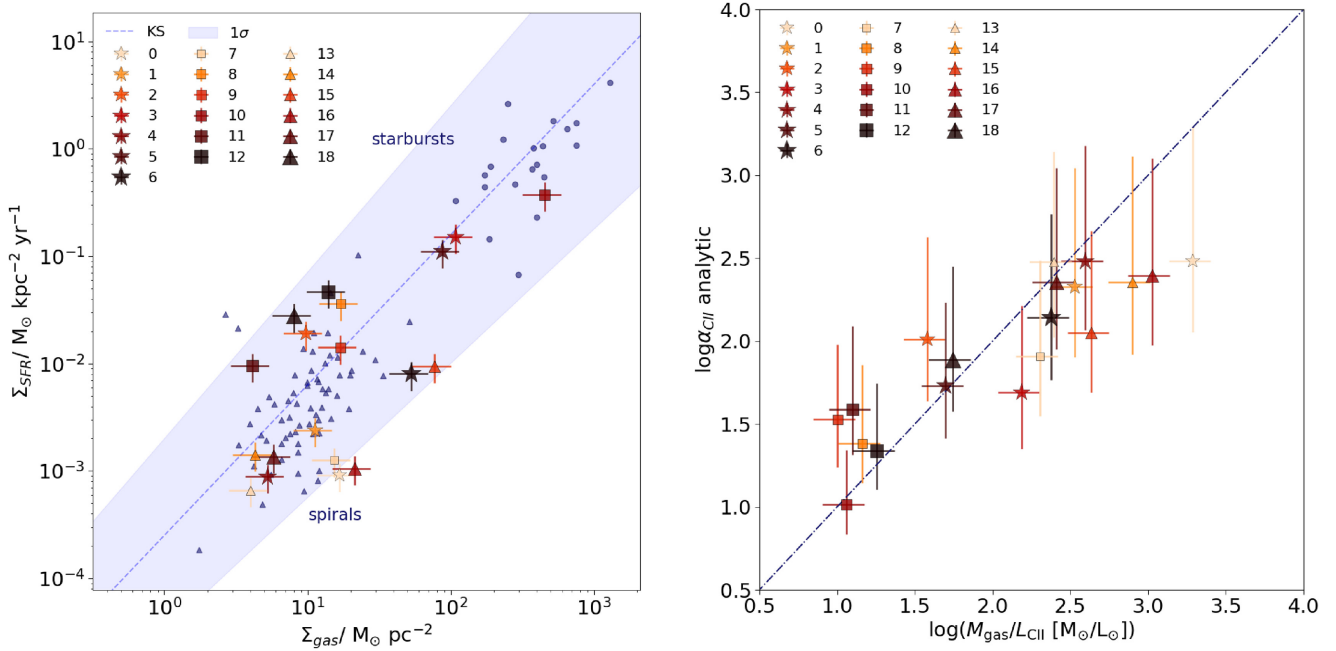


Figure 1. Left-hand panel: Measured Σ_{SFR} versus Σ_{gas} of our local sample. We associate with each galaxy an ID number that will be used in the following plots. The dashed blue line represents the **KS** relation (equation 3) and the blue shaded region its intrinsic scatter. Also shown for reference are a number of local spirals (black triangles, Kennicutt 1998) and starbursts (black stars, Kennicutt 1998). We distinguish each galaxy in our local sample with a different colour and identify them in the legend with their IDs as in Table 1. We also differentiate the three subsamples with a different shape: a (star), b (square), and c (triangle, all references are the same as in Table 1). We note galaxies in the local sample are consistent within errors with the **KS** relation. Right-hand panel: α_{CII} conversion factor computed from equation (5) versus the observed $\log(M_{\text{gas}}/L_{\text{CII}})$ for the same galaxies as in the left-hand panel. The solid symbols correspond to the value of α_{CII} obtained considering for each galaxy the κ_s value computed from the measured Σ_{SFR} and Σ_{gas} . The dotted dashed black line is the bisector, i.e. it represents the relation $\log \alpha_{\text{CII}} = \log(M_{\text{gas}}/L_{\text{CII}})$. The fact that the points lay within $\sim 1.5\sigma$ from the bisector shows that equation (2) gives a good estimate of the observed gas mass-to-[C II] luminosity ratio.

The **DL** relation (equation 2) has been derived from a portion of this same sample and therefore is nearly satisfied by construction. The galaxies in the local sample also follow the **KS** relation with a scatter consistent with that of local spirals and starbursts ($0.1 \leq \kappa_s \leq 5.9$; see Fig. 1, left-hand panel).

We compare the value of α_{CII} resulting from equation (5) with the ratio $M_{\text{gas}}/L_{\text{CII}}$ derived from observations (Fig. 1, right-hand panel). We find $0.7 \leq \log \alpha_{\text{CII}} \leq 3.2$. The predicted α_{CII} is consistent with the data at $<1.5\sigma$, although there are significant uncertainties.

Finally, we compare $T_{\text{d,CII}}$ and $T_{\text{d,SED}}$. For the local sample galaxies, we deduce $T_{\text{d,SED}}$ from the following equation:

$$\frac{F_{\nu_1}}{F_{\nu_2}} = \frac{\kappa_{\nu_1} [B_{\nu_1}(T_{\text{d,SED}}) - B_{\nu_1}(T_{\text{CMB}})]}{\kappa_{\nu_2} [B_{\nu_2}(T_{\text{d,SED}}) - B_{\nu_2}(T_{\text{CMB}})]}, \quad (16)$$

where we consider¹³ $\nu_1 = 1900$ GHz and $\nu_2 = (4285, 3409)$ GHz, corresponding to $\lambda_2 = (70, 88) \mu\text{m}$. This method based on the continuum fluxes ratio is equivalent to the single temperature grey-body SED fitting,¹⁴ hence the obtained dust temperature is indeed $T_{\text{d,SED}}$.

To produce $T_{\text{d,CII}}$, we consider a flat distribution for the burstiness parameter $0.1 \lesssim \kappa_s \lesssim 5.9$, where the range is derived from gas

masses and SFR measurements for the single sources (see Table 1). The temperature's comparison is shown in Fig. 2. We find that $T_{\text{d,CII}}$ and $T_{\text{d,SED}}$ are consistent within a 20 per cent uncertainty in ~ 90 per cent of the sources (precisely, all but galaxies ID11, ID18). The two discrepant sources are the most bursty ones in the sample, with an inferred $\kappa_s \sim 5$. Considering $\kappa_s \sim 5$ in these two cases (rather than the aforementioned flat distribution) would allow us to correctly recover $T_{\text{d,SED}}$ within 20 per cent uncertainty. Nevertheless, we have preferred to consider a flat distribution for κ_s to be more consistent with a general application at high- z , where this parameter is almost always unconstrained.

4 APPLICATION AT HIGH REDSHIFT

We now apply our method to high- z galaxies. We have collected a small (three galaxies) sample for which the properties (ii)–(vi) are measured. The high- z sample contains:

- (i) SPT 0418-47 (Weiß et al. 2013; Strandet et al. 2016): a strongly lensed dusty star-forming Galaxy (DSFG) at redshift $z = 4.225$.
- (ii) B1465666 (i.e. the ‘big three dragons’; Hashimoto et al. 2019): a Lyman Break Galaxy (LBG) at $z = 7.15$.
- (iii) MACS0416-Y1 (Tamura et al. 2019; Bakx et al. 2020): an LBG at $z \sim 8.31$.

The properties of these galaxies are summarized in Table 2. These sources are UV-selected, highly star forming (yet not extreme as $\text{SFR} \lesssim 500 M_{\odot} \text{yr}^{-1}$), do not host AGNs, and are presumably main-sequence high- z galaxies.

¹³We select these frequencies to avoid PAH contamination present at wavelengths $\lesssim 20 \mu\text{m}$. For ID10, we take $\nu_2 = 2998$ (100 μm) since observations at the above mentioned frequencies are not available.

¹⁴For all the sources where multiple continuum observations are available we also computed the full SED fitting, see Appendix B. We find $T_{\text{d,SED}}$ values fully consistent with that obtained from continuum fluxes ratio.

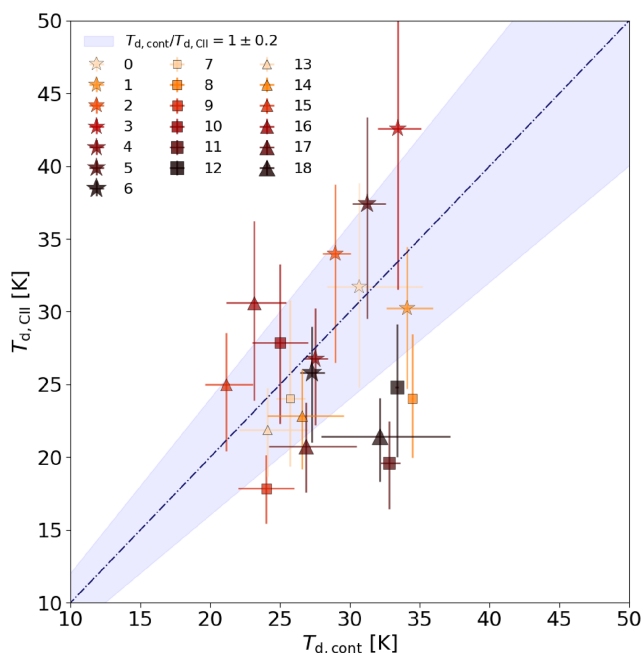


Figure 2. Comparison between $T_{d,CII}$ (from equation 12) and $T_{d,SED}$ (from equation 16) in our local template sample of galaxies (see Table 1 for the properties of each galaxy corresponding to the ID in legend). The dotted dashed grey line represents the relation $T_{d,CII} = T_{d,SED}$ and the shaded area represents a deviation from the equality of ± 20 per cent.

For all these sources, the parameter $y = r_{CII}/r_*$ has been estimated (Hashimoto et al. 2019; Bakx et al. 2020; Rizzo et al. 2020). Moreover, Rizzo et al. (2020) provided a constraint on Σ_{gas} for SPT 0418-47. Hence, we can also derive the burstiness parameter for this galaxy finding $\kappa_s \sim 9$. Due to the uncertainty in the gas mass derivation, in the computation we consider a Gaussian distribution centred around this value with a $\sigma \sim 2$ (i.e. we allow for values in the range $3 \lesssim \kappa_s \lesssim 15$, consistent with previous works; e.g. Vallini et al. 2020).

For the remaining two galaxies κ_s is unknown, hence we need to define a broader distribution of possible values for this parameter. High-redshift UV selected sources are strong UV emitters by construction, highly star forming, and consequently they are expected to be starburst $\kappa_s > 1$. Both locally and at intermediate redshift, values up to $\kappa_s \simeq 100$ have been observed in such galaxies (see e.g. Daddi et al. 2010). Recently, Vallini et al. (2020) for the mildly starbursting COS-3018 at $z = 6.854$ found $\kappa_s \sim 3$, applying the [C II]-emission model given in Ferrara et al. (2019). Applying the same method to B1465666 and MACS0416-Y1, Vallini (in preparation) finds very large values $30 \lesssim \kappa_s \lesssim 140$. Hence, we conservatively choose a random uniform distribution in the range $10 < \kappa_s < 100$ for these two sources.

Using equation (7), we compute the coefficient $\alpha_{CII,hz}$. We find $\alpha_{CII,hz} = 7^{+2}_{-1}$ for SPT 0418-47, which is consistent with the recent estimate by Rizzo et al. (2020) of $M_{gas}/L_{CII} \sim \alpha_{CII,hz} = 7 \pm 1$. We derive $\alpha_{CII,hz} = 2^{+2}_{-1}$ for B14-65666, and $\alpha_{CII,hz} = 2^{+2}_{-1}$ for MACS0416-Y1. We note that these values are lower than the average α_{CII} values found locally ($z \sim 0$; see e.g. Fig. 1). This might indicate a trend of less efficient [C II] emission per unit gas mass at higher redshift.

We now compare the $T_{d,CII}$ estimated by our model with the $T_{d,SED}$ from the SEDs. We summarize our findings and compare with literature data in Table 3 and Fig. 3. For SPT 0418-47, we derive $T_{d,CII} = 50^{+3}_{-5}$ K that is consistent, within the error, with the

$T_{d,SED}$ from the SED fitting by Strandet et al. (2016) ($T_{d,SED} = 45 \pm 2$ K). Recently, Reuter et al. (2020) derived a slightly higher dust temperature $T_{d,SED} = 58 \pm 11$ K for this source, which is still consistent with our result.¹⁵ Although the uncertainty of our $T_{d,CII}$ is larger than the one of $T_{d,SED}$ this is somewhat expected. The SED for SPT 0418-47 is well constrained, featuring data points on both sides of the FIR spectrum. On the other hand, the metallicity of the source is very uncertain, $0.3 \leq Z/Z_\odot \leq 1.3$, and this affects directly the error on our $T_{d,CII}$.

For B14-65666, we find $T_{d,CII} = 61^{+16}_{-15}$ K. This value is consistent with $T_{d,SED} = 48\text{--}61$ K, which is inferred considering $1.5 < \beta < 3.0$ (Hashimoto et al. 2019). For MACS0416-Y1 (Tamura et al. 2019; Bakx et al. 2020), we consider the upper limit on F_{v_0} recently derived by Bakx et al. (2020). Interestingly, $T_{d,CII}$ in equation (12) decreases with $f \propto F_{v_0}$. Hence, for this galaxy we provide an upper limit for the [C II] derived dust temperature: $T_{d,CII} \leq 82^{+16}_{-19}$ K. Very hot dust temperatures $T_{d,CII} > 120$ K are excluded thanks to the condition on SFR_{FIR} (see Section 2.3.1).¹⁶ This result is particularly relevant as Bakx et al. (2020) obtained only a lower limit for the dust temperature $T_{d,SED} \gtrsim 80$ K. By combining the two results, we can constrain the dust temperature of MACS0416-Y1 in the range $T_{d,SED} \sim 80\text{--}98$ K.

In conclusion, with our method, we can provide dust temperature estimations comparably accurate as that obtained from the traditional SED fitting with multiple bands data out to $z = 8.31$. This is very encouraging, as for the single high- z sources targeted by large programs, only single-band measurements are generally available. Hence, commonly used SED fitting is not applicable without some underlying restrictive assumption on $T_{d,SED}$. Our method can be used in these cases to improve the accuracy of the interpretation of FIR observations, and derive dust and galaxies properties.

4.1 Dust mass

Our method also provides reliable estimates of the dust masses of distant galaxies. Once α_{CII} has been determined, it is straightforward to derive M_d using equation (10). As already discussed, we discard the solutions for which $M_d > M_{d,max}$, which is computed in equation (15).

For SPT0418-47, we find $M_d = 1.2^{+0.3}_{-0.2} \times 10^8 M_\odot$, a value fully consistent with that obtained from SED fitting $M_d = 1.1^{+0.1}_{-0.2} \times 10^8 M_\odot$. For B14-65666, we find $M_d = 6.8^{+5.4}_{-2.4} \times 10^6 M_\odot$. This is also consistent with the result obtained from SED fitting by Hashimoto et al. (2019). They find $6.5 < M_d/10^6 M_\odot < 13.2$ with $1.5 \leq \beta \leq 2$. In the case of MACS0416-Y1, we find $M_d = 0.6^{+0.4}_{-0.2} \times 10^6 M_\odot$. This is consistent with the result obtained from SED fitting by Bakx et al. (2020). They find $M_d = 0.2\text{--}0.6 \times 10^6 M_\odot$ for $70 \text{ K} < T_{d,SED} < 130 \text{ K}$, and $\beta = 2$.

¹⁵Reuter et al. (2020) left $\lambda_* = 100 \mu\text{m}$ as an additional free parameter in the SED fitting (see also Spilker et al. 2016, for a detailed discussion), which resulted in a larger ($\times 4$) uncertainty alongside a raise in the dust temperature. The fewer FIR data currently available at very high- z do not allow for the application of a similar fitting procedure on a large scale. Hence, at the current stage a simpler grey-body (as in Strandet et al. 2016) with little variation in the dust properties is uniformly applied, leading to pretty consistent $T_{d,SED}$ derivations for different sources.

¹⁶Without the condition on SFR_{FIR} dust temperatures as large as $T_{d,CII} \gtrsim 130$ K would be reached. In part, this is a consequence of the very large uncertainty (~ 80 per cent) on the already low metallicity of this galaxy ($Z = 0.2 Z_\odot$). Indeed for a fixed flux F_{v_0} , $T_{d,CII}$ diverges as the metallicity $Z \rightarrow 0$ as this is equivalent to $M_d \rightarrow 0$, see equation (10).

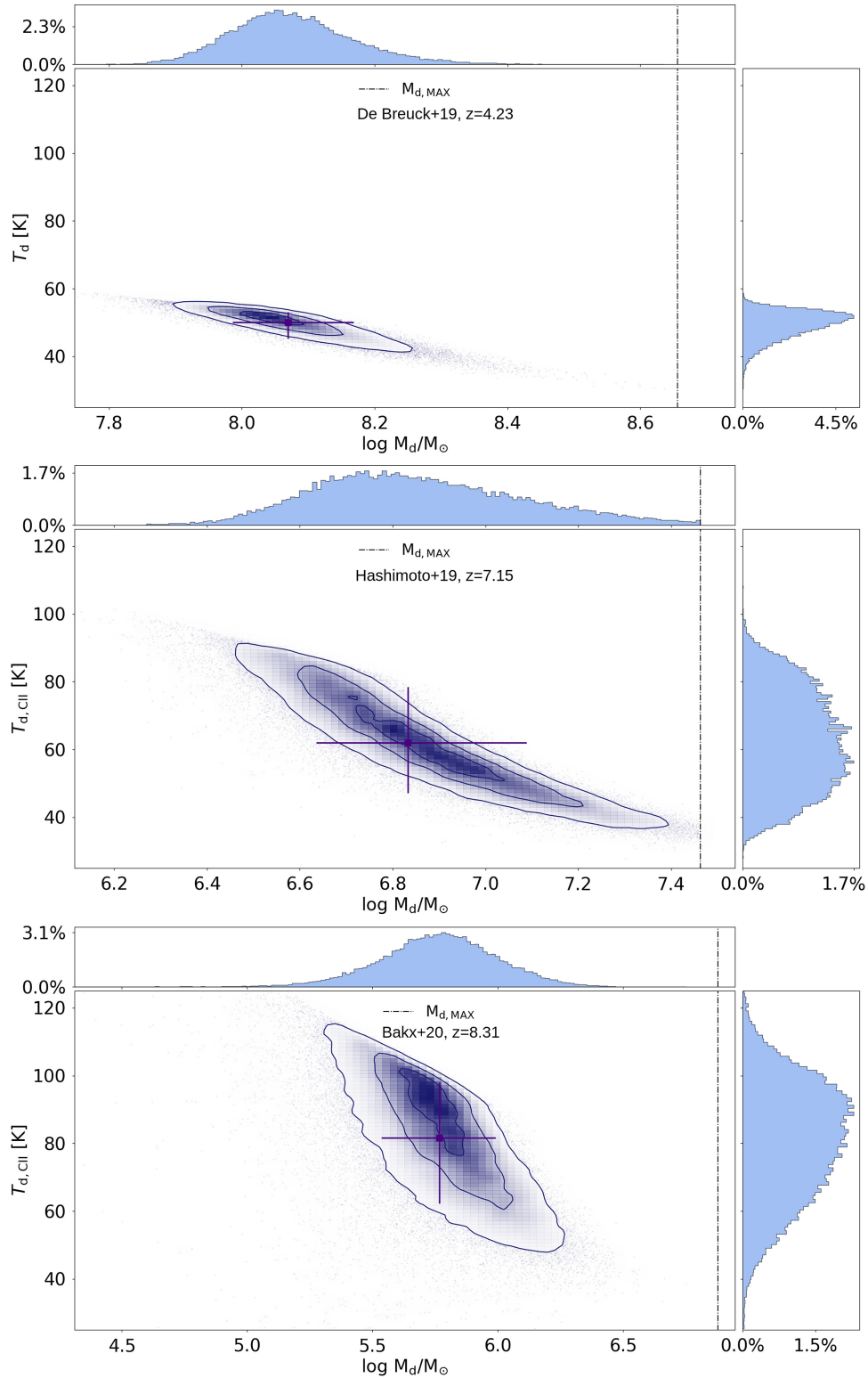


Figure 3. Recovered distribution of $T_{d,CII}$ as a function of M_d for the galaxies in our high- z template sample (same order as in Table 2). The contours show the (16, 50, 84) percentiles of the distribution. The median value is represented by the purple square (alongside its 16 and 84 percentiles marked by the error bars). We also show the temperature (right) and mass (top) PDFs. The upper limit on the dust mass, computed through equation (15), is shown by the vertical black dot-dashed line in each panel.

Table 2. Properties of our high- z template sample of galaxies. We underline that for the data where the uncertainty is not given we consider a 30 per cent relative error which is a conservative choice given the other available data.

Galaxy	z	F_{ν_0} (mJy)	Z (Z_{\odot})	$\log \Sigma_{\text{SFR}}$ ($\text{M}_{\odot} \text{ yr}^{-1} \text{ kpc}^{-2}$)	L_{CII} ($10^8 L_{\odot}$)	κ_s	$y = r_{\text{CII}}/r_*$	M_* ($10^8 M_{\odot}$)
SPT0418-47 ^a	4.23	3.3 ± 0.3	$0.30 - 1.30$	1.72	19.9 ± 1.5	9	1.5	120.0 ± 15.0
B1465666 ^b	7.15	0.13 ± 0.03	0.40 ± 0.30	1.32	11.0 ± 1.4	—	1.4 ± 0.4	7.7
MACS0416-Y1 ^c	8.31	<0.02	0.20 ± 0.16	1.16	1.4 ± 0.2	—	1.2 ± 0.4	2.0

^aBothwell et al. (2017); De Breuck et al. (2019); Reuter et al. (2020); Rizzo et al. (2020). Here, we show the intrinsic values, which are obtained by dividing by the magnification factor of the source $\mu = 32.7$ (De Breuck et al. 2019).

^bHashimoto et al. (2019).

^cBakx et al. (2020).

Table 3. Comparison between predicted (‘this work’) and published properties of galaxies in our high- z sample. We underline that the dust temperature estimates taken from the literature are obtained through SED fitting, while our predictions correspond to $T_{\text{d,CII}}$.

Galaxy	$\alpha_{\text{CII, hz}}$	$T_{\text{d,SED}}$ (K)	$T_{\text{d,CII}}$ (K)	M_{d} ($10^6 M_{\odot}$)	y_{d} ($\text{M}_{\odot}/\text{SN}$)
SPT0418-47 ^a	7 ± 1	45–58	—	110^{+10}_{-20}	—
This work	7^{+2}_{-1}	—	50^{+3}_{-5}	118^{+30}_{-20}	0.5 ± 0.1
B1465666 ^b	—	48–61	—	6.5–13.2	—
This work	2^{+2}_{-1}	—	61^{+16}_{-15}	$6.8^{+5.4}_{-2.4}$	$0.5^{+0.3}_{-0.1}$
MACS0416Y1 ^c	—	≥ 80	—	0.2–0.6	—
This work	2^{+2}_{-1}	—	$\leq 82^{+16}_{-19}$	$0.6^{+0.4}_{-0.2}$	0.2 ± 0.1

^aStrandet et al. (2016); Bothwell et al. (2017); De Breuck et al. (2019); Reuter et al. (2020); Rizzo et al. (2020). Here, we show the intrinsic values, which are obtained by dividing by the magnification factor of the source $\mu = 32.7$ (De Breuck et al. 2019).

^bHashimoto et al. (2019).

^cBakx et al. (2020).

We also compute the dust yield per SN, y_{d} , required to produce the above dust masses, which are consistent with previous estimates in the literature. We use the formula in Sommovigo et al. (2020): $y_{\text{d}} = M_{\text{d}}/M_{*}\nu_{\text{SN}}$, where $\nu_{\text{SN}} = (53 M_{\odot})^{-1}$ is the number of SNe per solar mass of stars formed (Ferrara & Tolstoy 2000). For all the three sources it is $y_{\text{d}} \lesssim 1 M_{\odot}$ (see Table 3 for the value of y_{d} in each galaxy), i.e. within the allowed range given in the latest SNe dust production studies by Leńniewska & Michałowski (2019). They find that up to $y_{\text{d}} \leq 1.1 M_{\odot}$ per SN can be produced, where the exact value depends on the amount of dust which is destroyed during the explosion ($1.1 M_{\odot}$ corresponds to the extreme case of no dust destruction).

The presence of warmer dust ($T_{\text{d,SED}} \gtrsim 50$ K) in these high- z sources alleviates the large dust mass requirements set by the observed FIR luminosity. This is particularly relevant in the context of early galaxies. Allowing for lower dust masses prevents from invoking super efficient dust production by stellar sources, which is difficult to reconcile with both data and theoretical models (for a detailed discussion, see e.g. Sommovigo et al. 2020).

5 MOLECULAR GAS CONTENT

Besides providing a reliable determination of the dust temperature, our method offers a physical interpretation of the Zanella et al. (2018) relation. To show this, we parallel the analysis in Section 2.2. Here, we substitute the KS relation with the following expression linking the star formation and molecular gas surface density Σ_{H_2} (Krumholz

2015):¹⁷

$$\Sigma_{\text{SFR}} = 10^{-9} \frac{\Sigma_{\text{H}_2}}{t_{\text{depl}}}, \quad (17)$$

where t_{depl} is the depletion time. Combining equation (17) with the DL relation and the definition of the molecular conversion factor, $\alpha_{\text{CII, mol}} = \Sigma_{\text{H}_2}/\Sigma_{\text{CII}}$, we find

$$\alpha_{\text{CII, mol}} = \frac{t_{\text{depl}}}{3.3 \times 10^{-2}} \Sigma_{\text{SFR}}^{-0.075}. \quad (18)$$

The dependence of $\alpha_{\text{CII, mol}}$ on Σ_{SFR} is extremely weak, in contrast with $\alpha_{\text{CII}} \propto \Sigma_{\text{SFR}}^{-0.3}$ (total gas conversion coefficient,¹⁸ see Section 2.2). We can understand this result in physical terms as both Σ_{H_2} and Σ_{CII} scale almost linearly with Σ_{SFR} , their ratio is virtually independent of this quantity. Instead, the total gas reservoir is less sensitive to star formation (see equation 3). Therefore, in the ratio $\Sigma_{\text{gas}}/\Sigma_{\text{CII}}$ the dependence on Σ_{SFR} does not cancel out.

Most recent results by Walter et al. (2020) suggest that t_{depl} is nearly constant above redshift $z > 2$, and then increases slightly from $t_{\text{depl}} \sim 0.4$ Gyr at $z \sim 2$, to $t_{\text{depl}} \sim 0.7$ Gyr at $z = 0$. Substituting these values in equation (18), we find $\alpha_{\text{CII, mol}} = (12 - 21) \Sigma_{\text{SFR}}^{-0.075}$. This result is compatible with the measurement of $M_{\text{H}_2}/L_{\text{CII}} = 31^{+31}_{-16} M_{\odot}/L_{\odot}$ derived by Zanella et al. (2018) in a sample of galaxies at $z \sim 0-6$. Recently, Dessauges-Zavadsky et al. (2020) found this $M_{\text{H}_2}/L_{\text{CII}}$ ratio to hold also in the [CII]-detected galaxies at $z \sim 4-6$ targeted by the ALPINE survey, albeit with some uncertainties.¹⁹

On average, previous works indicated longer depletion times $t_{\text{depl}} \sim [0.5, 2]$ Gyr both in local and high- z galaxies ($z \sim 6-0$; see e.g. Bigiel et al. 2008; Daddi et al. 2010; Genzel et al. 2010, 2015; Leroy et al. 2013; Sargent et al. 2014; Béthermin et al. 2015; Dessauges-Zavadsky et al. 2015, 2020; Schinnerer et al. 2016; Saintonge et al. 2017; Scoville et al. 2017). Nevertheless, the observed scatter in t_{depl} is within measurement errors by Zanella et al. (2018). The variation of $\alpha_{\text{CII, mol}}$ is significantly smaller than that of α_{CII} . Already within our limited sample of 23 galaxies, α_{CII} varies by nearly two orders of magnitude due to its strong dependence on Σ_{SFR} and κ_s (see Fig. 1).

¹⁷We adopt the standard units used for these quantities: $\Sigma_{\text{SFR}} [M_{\odot} \text{ kpc}^{-2} \text{ yr}^{-1}]$, $t_{\text{depl}} [\text{Gyr}]$, and in equation (18), $\alpha_{\text{CII, mol}} [M_{\odot}/L_{\odot}]$.

¹⁸The exponent -0.3 is an average value between the -0.36 and -0.29 found in equations (5) and (7).

¹⁹More precisely, Dessauges-Zavadsky et al. (2020) find a good agreement between molecular gas masses derived from [CII] luminosities (using the relation by Zanella et al. 2018), dynamical masses, and rest-frame 850 μm luminosities (extrapolated from the rest-frame 158 μm continuum).

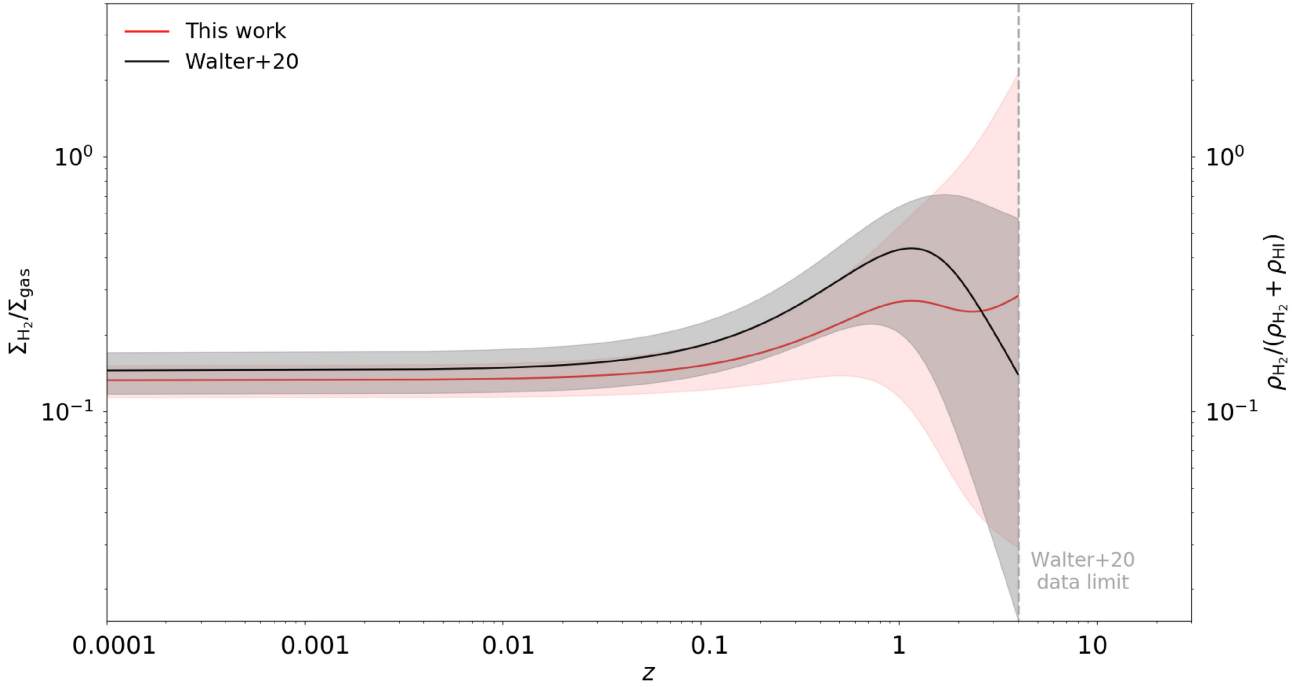


Figure 4. Redshift evolution of the molecular gas fraction $f_{\text{H}_2}(z) = \Sigma_{\text{H}_2}/\Sigma_{\text{gas}}$. The red line represents our fiducial estimate. The black line shows the $\rho_{\text{H}_2}/(\rho_{\text{H}_2} + \rho_{\text{HI}})$ trend observed by Walter et al. (2020) and the vertical grey dashed line refers to the highest redshift considered in their analysis. For sake of the comparison, here we consider the same $t_{\text{depl}}(z)$ as in Walter et al. (2020).

5.1 Molecular gas fraction

Armed with the expressions for α_{CII} (equation 5) and $\alpha_{\text{CII},\text{mol}}$ (equation 18) we intend to study the redshift evolution of the ratio $\alpha_{\text{CII},\text{mol}}/\alpha_{\text{CII}} = \Sigma_{\text{H}_2}/\Sigma_{\text{gas}}$. To this aim, since $\alpha_{\text{CII}} \propto \Sigma_{\text{SFR}}^{-0.3}$, we need to provide a qualitative prescription for the redshift evolution of the average $\bar{\Sigma}_{\text{SFR}}(z)$ in normal galaxies.

We consider the cosmic SFR comoving density, ψ , derived by Madau & Dickinson (2014) in the range $z = 0.01$ –8. We combine ψ with the evolution of the effective radius, $r_* \approx r_e = 6.9 \times (1+z)^{1.2}$ kpc, derived by Shibuya, Ouchi & Harikane (2015) for an *HST* sample of $\sim 19\,000$ galaxies at $z = 0$ –10 to obtain $\bar{\Sigma}_{\text{SFR}}(z) = \psi/\pi r_e^2$, and the corresponding expression for $\alpha_{\text{CII}}(z)$ from equation (5).

For simplicity, in computing $\alpha_{\text{CII}}(z)$ we consider $\kappa_s = 1$ as on average we expect most local and low- z galaxies to lie on the KS relation.²⁰ In parallel to the result shown in Section 5, we write $\alpha_{\text{CII},\text{mol}}(z) = (12\text{--}21) \bar{\Sigma}_{\text{SFR}}^{-0.075}$. We can then compute the ratio:

$$f_{\text{H}_2}(z) \equiv \Sigma_{\text{H}_2}/\Sigma_{\text{gas}} = \alpha_{\text{CII},\text{mol}}/\alpha_{\text{CII}} \sim \left(\frac{\bar{\Sigma}_{\text{SFR}}}{\text{M}_{\odot} \text{ kpc}^{-2} \text{ yr}^{-1}} \right)^{0.225}. \quad (19)$$

The redshift evolution of the molecular fraction in galaxies has been experimentally determined by Walter et al. (2020) from observations²¹ of molecular, ρ_{H_2} , and atomic, ρ_{HI} , gas densities at

$z \lesssim 4$. In Fig. 4, we show the comparison of $f_{\text{H}_2}(z)$ with the observed redshift evolution of the empirical $\rho_{\text{H}_2}/(\rho_{\text{H}_2} + \rho_{\text{HI}})$ ratio.

The two approaches yield a pretty consistent evolution trend, albeit they are both affected by large uncertainties. We find that on average $f_{\text{H}_2}(z)$ increases by a factor of ~ 2 from $z = 0.01$ to $z = 1$, in agreement with the trend found by Walter et al. (2020) (~ 1.7 –3.6). However, at $z > 1$ the two trends might be different, as we predict a possible further increase in $f_{\text{H}_2}(z)$. This can be due to (i) a further increase in the $M_{\text{H}_2}/M_{\text{gas}}$, and/or (ii) an increase in the ratio $r_{\text{gas}}/r_{\text{H}_2}$ ratio. The first case seems to be disfavoured by theoretical studies (see e.g. Davé et al. 2017), as both the H_2 and HI evolution become steeper with redshift at fixed stellar mass. The second possibility is instead suggested by recent works showing the presence of $[\text{CII}]$ emission at high- z around $\times 1.5$ –3 times more extended than the stellar (and possibly molecular) mass (see e.g. Carniani et al. 2017, 2018a; Fujimoto et al. 2019, 2020; Carniani et al. 2020; Ginolfi et al. 2020). Clarifying this uncertainty is crucial as the assumption that $f_{\text{H}_2} \approx 1$ at high- z is widely used to derive molecular gas masses from dynamical (Daddi et al. 2010; Genzel et al. 2010; Dessauges-Zavadsky et al. 2020) and dust (Scoville et al. 2016; Dessauges-Zavadsky et al. 2020) masses.

6 SUMMARY AND CONCLUSIONS

We have proposed a novel method to derive the dust temperature in galaxies, based on the combination of continuum and $[\text{CII}]$ line emission measurements, which breaks the SED fitting degeneracy between dust mass and temperature. The method allows constraining T_d from a single-band observation at 1900 GHz (rest frame). We conveniently provide analytical expressions in equation (12) for a direct application.

Besides, the same method offers a physical explanation for the empirical relation found by Zanella et al. (2018) between $[\text{CII}]$ lumi-

²⁰If $\kappa_s > 1$ the $\Sigma_{\text{H}_2}/\Sigma_{\text{gas}}$ curve is shifted upwards, as we are reducing $\Sigma_{\text{gas}} \propto \alpha_{\text{CII}} \propto \kappa_s^{-5/7}$, without affecting Σ_{H_2} . Hence, at higher redshift deviations are expected to occur due to the burstiness of galaxies.

²¹The HI density is obtained by combining measurements of HI emission in the local universe (see e.g. Zwaan et al. 2005) with quasar absorption lines at higher z (see e.g. Prochaska & Wolfe 2009); $\rho_{\text{H}_2}(z)$ determination is based on CO and FIR dust continuum data (e.g. reviews by Carilli & Walter 2013; Hodge & da Cunha 2020; Péroux & Howk 2020; Tacconi, Genzel & Sternberg 2020).

osity and molecular gas. We also derive the relation between total gas surface density and [C II] surface brightness, $\Sigma_{\text{gas}} = \alpha_{\text{C II}} \Sigma_{\text{C II}}$. By combining such relations, we predict the redshift evolution of the molecular gas fraction defined here as $\Sigma_{\text{H}_2} / \Sigma_{\text{gas}}$.

We summarize our main findings below:

(i) **Dust temperature from [C II] data at high-*z*:** Using a single-band observation, with our method, we can constrain the dust temperature as well as with the commonly used SED fitting in multiple bands. We recover dust temperatures consistent with literature data (within 1σ) out to redshift $z = 8.31$.

(ii) **Gas-to-[C II] luminosity relation:** The total gas conversion coefficient $\alpha_{\text{C II}}$ strongly depends on the SFR surface density ($\sim \Sigma_{\text{SFR}}^{1/3}$) and the burstiness of galaxies (see equation 5). When computing the analogous conversion factor for the molecular gas $\alpha_{\text{C II, mol}}$, we find that the dependence on Σ_{SFR} nearly cancels out, hence $\alpha_{\text{C II, mol}} \approx \text{const.}$ (see equation 18).

(iii) **Molecular gas fraction:** We find that $f_{\text{H}_2}(z)$ on average increases with z by a factor ≈ 2 from $z = 0.01$ to $z = 1$. This is consistent with the trend observed by Walter et al. (2020). We predict a possible further increase at $z > 1$. This could be caused by a rise of the H_2 content, and/or a change in the relative extension of H_2 and H I gas.

Assuming a dust temperature, as usually done in high-*z* galaxy observation analysis, introduces large uncertainties on the derived dust masses, infrared luminosities, and SFRs (see also e.g. Sommovigo et al. 2020 for a detailed discussion). Our method can improve the reliability of the interpretation of [C II] and continuum observations from ALMA and NOEMA. This is particularly relevant in the context of recent ALMA large programs targeting [C II] emitters at high-*z*, such as ALPINE (Le Fèvre et al. 2019; Béthermin et al. 2020; Schaerer et al. 2020), REBELS (PI: Bouwens), and others. With future instruments such as *JWST*, providing more accurate metallicity measurements, it will be possible to improve current estimates of the dust-to-gas ratios at high-*z*. This will further enhance the precision of our dust temperature determinations.

ACKNOWLEDGEMENTS

LS, AF, SC, AP, and LV acknowledge support from the ERC Advanced Grant INTERSTELLAR H2020/740120 (PI: Ferrara). Any dissemination of results must indicate that it reflects only the author's view and that the Commission is not responsible for any use that may be made of the information it contains. Partial support from the Carl Friedrich von Siemens-Forschungspreis der Alexander von Humboldt-Stiftung Research Award is kindly acknowledged (AF). We thank R. Kennicutt, T. Díaz-Santos, and C. De Breuck for the useful discussions, and for the help in retrieving the data from their surveys, respectively, KINGFISH, GOALS, and SPT. We also thank the referee C. De Breuck for the useful comments.

7 DATA AVAILABILITY

Part of the data underlying this article were accessed from the computational resources available to the Cosmology Group at Scuola Normale Superiore, Pisa (IT). The derived data generated in this research will be shared on reasonable request to the corresponding author.

REFERENCES

Baer M., Camps P., 2015, *Astron. Comput.*, 12, 33
Bakx T. J. L. C. et al., 2020, *MNRAS*, 493, 4294

Barisic I. et al., 2017, *ApJ*, 845, 41
Behrens C., Pallottini A., Ferrara A., Gallerani S., Vallini L., 2018, *MNRAS*, 477, 552
Bigiel F., Leroy A., Walter F., Brinks E., de Blok W. J. G., Madore B., Thornley M. D., 2008, *AJ*, 136, 2846
Bothwell M. S. et al., 2017, *MNRAS*, 466, 2825
Bouwens R. J. et al., 2016, *ApJ*, 833, 72
Bovino S., Latif M. A., Grassi T., Schleicher D. R. G., 2014, *MNRAS*, 441, 2181
Bowler R. A. A., Bourne N., Dunlop J. S., McLure R. J., McLeod D. J., 2018, *MNRAS*, 481, 1631
Bradač M. et al., 2017, *ApJ*, 836, L2
Béthermin M. et al., 2015, *A&A*, 573, A113
Béthermin M. et al., 2020, *A&A*, 643, A2
Caldú-Primo A., Cruz-González I., 2008, Massive Star Formation in Two Spiral Galaxies: NGC 3938 and NGC 3184; Multiwavelength Analysis, Revista Mexicana de Astronomía y Astrofísica Conference Series, Vol. 34, p. 115
Calzetti D., Armus L., Bohlin R. C., Kinney A. L., Koornneef J., Storchi-Bergmann T., 2000, *ApJ*, 533, 682
Camps P., Baer M., 2015, *Astron. Comput.*, 9, 20
Capak P. L. et al., 2015, *Nature*, 522, 455
Carilli C. L., Walter F., 2013, *ARA&A*, 51, 105
Carniani S., Maiolino R., Smit R., Amorín R., 2018b, *ApJ*, 854, L7
Carniani S. et al., 2017, *A&A*, 605, A42
Carniani S. et al., 2018a, *MNRAS*, 478, 1170
Carniani S. et al., 2020, *MNRAS*, 499, 5136
Casey C. M., 2012, *MNRAS*, 425, 3094
Casey C. M., Hodge J., Zavala J. A., Spilker J., da Cunha E., Staguhn J., Finkelstein S. L., Drew P., 2018, *ApJ*, 862, 78
Chevallard J. et al., 2019, *MNRAS*, 483, 2621
Chu J. K. et al., 2017, *ApJS*, 229, 25
Cormier D. et al., 2019, *A&A*, 626, A23
da Cunha E. et al., 2013, *ApJ*, 766, 13
Daddi E. et al., 2010, *ApJ*, 714, L118
Davé R., Rafieeantsoa M. H., Thompson R. J., Hopkins P. F., 2017, *MNRAS*, 467, 115
Dayal P., Ferrara A., 2018, *Phys. Rep.*, 780, 1
Dayal P., Hirashita H., Ferrara A., 2010, *MNRAS*, 403, 620
De Breuck C. et al., 2019, *A&A*, 631, A167
Decataldo D., Lupi A., Ferrara A., Pallottini A., Fumagalli M., 2020, *MNRAS*, 497, 4718
De Looze I. et al., 2014, *A&A*, 568, A62 (DL)
Dessauges-Zavadsky M. et al., 2015, *A&A*, 577, A50
Dessauges-Zavadsky M. et al., 2020, *A&A*, 643, A5
De Vis P. et al., 2019, *A&A*, 623, A5
Di Mascia F. et al. 2021, *MNRAS*, 503, 2349/mnras/stab528
Draine B. T., 1989, *Infrared Spectroscopy in Astronomy*, ESA: European Space Agency
Draine B. T., 2003, *ARA&A*, 41, 241
Draine B. T., 2004, *The Cold Universe*. Springer-Verlag, Berlin, p. 213
Draine B. T., Li A., 2007, *ApJ*, 657, 810
Engelbracht C. W., Rieke G. H., Gordon K. D., Smith J.-D. T., Werner M. W., Moustakas J., Willmer C. N. A., Vanzì L., 2008, *ApJ*, 678, 804
Ferland G. J. et al., 2017, *Rev. Mex. Astron. Astrofis.*, 53, 385
Fernandez-Ontiveros J., Spinoglio L., Pereira-Santaella M., Malkan M., Andreani P., Dasyra K., 2016, *The Astrophysical Journal Supplement Series*, 226, 19
Ferrara A., Tolstoy E., 2000, *MNRAS*, 313, 291
Ferrara A., Vallini L., Pallottini A., Gallerani S., Carniani S., Kohandel M., Decataldo D., Behrens C., 2019, *MNRAS*, 489, 1
Fixsen D. J., 2009, *ApJ*, 707, 916
Fujimoto S. et al., 2019, *ApJ*, 887, 107
Fujimoto S. et al., 2020, *ApJ*, 900, 1
Galametz M., Madden S. C., Galliani F., Hony S., Bendo G. J., Sauvage M., 2011, *A&A*, 532, A56
Gallerani S., Pallottini A., Feruglio C., Ferrara A., Maiolino R., Vallini L., Riechers D. A., Pavesi R., 2017, *MNRAS*, 473, 1909
Galliano F., Dwek E., Chianali P., 2008, *ApJ*, 672, 214

- Galliano F., Madden S. C., Jones A. P., Wilson C. D., Bernard J.-P., 2005, *A&A*, 434, 867
- Genzel R. et al., 2010, *MNRAS*, 407, 2091
- Genzel R. et al., 2015, *ApJ*, 800, 20
- Ginolfi M. et al., 2020, *A&A*, 633, A90
- Grassi T., Bovino S., Schleicher D. R. G., Prieto J., Seifried D., Simoncini E., Gianturco F. A., 2014, *MNRAS*, 439, 2386
- Groves B. A. et al., 2015, *ApJ*, 799, 96
- Harikane Y. et al., 2018, *ApJ*, 859, 84
- Hashimoto T. et al., 2019, *PASJ*, 71, 71
- Hayes M. et al., 2014, *ApJ*, 782, 6
- Heiderman A., Evans N. J., Allen L. E., Huard T., Heyer M., 2010, *ApJ*, 723, 1019
- Herrera-Camus R. et al., 2015, *ApJ*, 800, 1
- Hodge J. A., da Cunha E., 2020, *R. Soc. Open Sci.*, 7, 200556
- James A., Dunne L., Eales S., Edmunds M. G., 2002, *MNRAS*, 335, 753
- Jarrett T. H., Chester T., Cutri R., Schneider S. E., Huchra J. P., 2003, *AJ*, 125, 525
- Jones T., Sanders R., Roberts-Borsani G., Ellis R. S., Laporte N., Treu T., Harikane Y., 2020, *ApJ*, 903, 150
- Kennicutt R. C. et al., 2011, *PASP*, 123, 1347
- Kennicutt R. C. Jr., 1998, *ApJ*, 498, 541
- Kennicutt R. C., Jr. et al., 1998, *ApJ*, 498, 181 (KS)
- Knudsen K. K., Watson D., Frayer D., Christensen L., Gallazzi A., Michałowski M. J., Richard J., Zavala J., 2016, *MNRAS*, 466, 138
- Kohandel M., Pallottini A., Ferrara A., Zanella A., Behrens C., Carniani S., Gallerani S., Vallini L., 2019, *MNRAS*, 487, 3007
- Krumholz M. R., 2015, Notes on Star Formation, preprint ([arXiv:1511.03457](https://arxiv.org/abs/1511.03457))
- Laporte N. et al., 2017, *ApJ*, 837, L21
- Laporte N. et al., 2019, *MNRAS*, 487, L81
- Le Fèvre O. et al., 2019, preprint ([arXiv:1910.09517](https://arxiv.org/abs/1910.09517))
- Leroy A. K., Walter F., Brinks E., Bigiel F., de Blok W. J. G., Madore B., Thornley M. D., 2008, *AJ*, 136, 2782
- Leroy A. K. et al., 2011, *ApJ*, 737, 12
- Leroy A. K. et al., 2013, *AJ*, 146, 19
- Leńniewska A., Michałowski M. J., 2019, *A&A*, 624, L13
- Madau P., Dickinson M., 2014, *ARA&A*, 52, 415
- Madden S. C. et al., 2014, *PASP*, 126, 1079
- Madden S. C. et al., 2020, *A&A*, 643, A141
- Maiolino R., Mannucci F., 2019, *A&AR*, 27, 3
- Maiolino R. et al., 2015, *MNRAS*, 452, 54
- Matthee J. et al., 2017, *ApJ*, 851, 145
- Matthee J. et al., 2019, *ApJ*, 881, 124
- Ma X., Hopkins P. F., Faucher-Giguère C.-A., Zolman N., Muratov A. L., Kereš D., Quataert E., 2016, *MNRAS*, 456, 2140
- Meurer G. R., Heckman T. M., Calzetti D., 1999, *ApJ*, 521, 64
- Nilson P., 1973, *Nova Acta Regiae Soc. Sci. Upsaliensis Ser. V*
- Östlin G. et al., 2014, *ApJ*, 797, 11
- Pallottini A., Ferrara A., Bovino S., Vallini L., Gallerani S., Maiolino R., Salvadori S., 2017b, *MNRAS*, 471, 4128
- Pallottini A., Ferrara A., Gallerani S., Vallini L., Maiolino R., Salvadori S., 2017a, *MNRAS*, 465, 2540
- Pallottini A. et al., 2019, *MNRAS*, 487, 1689
- Pentericci L. et al., 2016, *ApJ*, 829, L11
- Pereira-Santaella M., Rigopoulou D., Farrah D., Leboutteiller V., Li J., 2017, *MNRAS*, 470, 1218
- Pizzati E., Ferrara A., Pallottini A., Gallerani S., Vallini L., Decataldo D., Fujimoto S., 2020, *MNRAS*, 495, 160
- Planck Collaboration VI, 2020, *A&A*, 641, A6
- Prochaska J. X., Wolfe A. M., 2009, *ApJ*, 696, 1543
- Puschnig J. et al., 2020, *A&A*, 644, A10
- Péroux C., Howk J. C., 2020, *ARA&A*, 58, 363
- Reuter C. et al., 2020, *ApJ*, 902, 78
- Rizzo F., Vegetti S., Powell D., Fraternali F., McKean J. P., Stacey H. R., White S. D. M., 2020, *Nature*, 584, 201
- Rosdahl J., Blaizot J., Aubert D., Stranex T., Teyssier R., 2013, *MNRAS*, 436, 2188
- Rémy-Ruyer A. et al., 2014, *A&A*, 563, A31
- Saintonge A. et al., 2017, *ApJS*, 233, 22
- Sargent M. T. et al., 2014, *ApJ*, 793, 19
- Schaerer D. et al., 2020, *A&A*, 643, A3
- Schinnerer E. et al., 2016, *ApJ*, 833, 112
- Scoville N. et al., 2016, *ApJ*, 820, 83
- Scoville N. et al., 2017, *ApJ*, 837, 150
- Shibuya T., Ouchi M., Harikane Y., 2015, *ApJS*, 219, 15
- Smit R. et al., 2018, *Nature*, 553, 178
- Sommovigo L., Ferrara A., Pallottini A., Carniani S., Gallerani S., Decataldo D., 2020, *MNRAS*, 497, 956
- Spilker J. S. et al., 2016, *ApJ*, 826, 112
- Stacey G. J., Geis N., Genzel R., Lugten J. B., Poglitsch A., Sternberg A., Townes C. H., 1991, *ApJ*, 373, 423
- Strandet M. L. et al., 2016, *ApJ*, 822, 80
- Tacconi L. J., Genzel R., Sternberg A., 2020, *ARA&A*, 58, 157
- Tamura Y. et al., 2019, *ApJ*, 874, 27
- Teyssier R., Pontzen A., Dubois Y., Read J. I., 2013, *MNRAS*, 429, 3068
- Torrey P. et al., 2019, *MNRAS*, 484, 5587
- Vallini L., Ferrara A., Pallottini A., Carniani S., Gallerani S., 2020, *MNRAS*, 495, L22
- Vallini L., Ferrara A., Pallottini A., Gallerani S., 2017, *MNRAS*, 467, 1300
- Vallini L., Gallerani S., Ferrara A., Pallottini A., Yue B., 2015, *ApJ*, 813, 36
- Walter F. et al., 2016, *ApJ*, 833, 67
- Walter F. et al., 2020, *ApJ*, 902, 111
- Weingartner J. C., Draine B. T., 2001, *ApJ*, 548, 296
- Weiß A. et al., 2013, *ApJ*, 767, 88
- Willott C. J., Carilli C. L., Wagg J., Wang R., 2015, *ApJ*, 807, 180
- Wolfe M. G., McKee C. F., Hollenbach D., Tielens A. G. G. M., 2003, *ApJ*, 587, 278
- Wright S. A., Law D. R., Ellis R. S., Erb D. K., Larkin J. E., Lu J. R., Steidel C. C., 2010, The Astronomy and Astrophysical Decadal Survey. Science White paper
- Zanella A. et al., 2018, *MNRAS*, 481, 1976
- Zwaan M. A., Meyer M. J., Staveley-Smith L., Webster R. L., 2005, *MNRAS*, 359, L30

APPENDIX A: HINTS FROM SIMULATIONS

The method developed in this paper can reliably determine the dust temperature in a galaxy for which only a *single* simultaneous observation for the [C II] line and underlying continuum is available. This value corresponds to the canonical temperature, $T_{\text{d,SED}}$, that one would normally define from fitting the SED with a single temperature grey-body formula. As already mentioned, $T_{\text{d,SED}}$ does not necessarily correspond to the physical dust temperature which instead is distributed according to a given PDF (see e.g. Behrens et al. 2018; Sommovigo et al. 2020; Di Mascia et al. 2021). Hence, it is instructive to understand the relation among $T_{\text{d,SED}}$ and the PDF properties.

In the context of theoretical studies, i.e. both analytical models and simulations, the dust temperature PDF is actually available. Various weighting procedures can be applied to this PDF, and then the average can be compared to the observational results. In particular, the most commonly adopted are the mass- (M-weighted) and luminosity-weighted (L-weighted; $L \propto M_{\text{d}} T_{\text{d}}^{4+\beta}$). The M-weighted temperature traces the most abundant cold temperature component; instead, the L-weighted is biased towards hotter but less massive dust component present in star-forming regions where it is efficiently heated by the UV emission from newborn stars (see e.g. Behrens et al. 2018; Sommovigo et al. 2020; G137). Neither of them is traced by $T_{\text{d,SED}}$. Indeed cold dust nearly in equilibrium with the CMB is not observable in emission; hot dust (if present) emits mainly in the MIR, where it is largely responsible for distortions of the single-temperature grey body (see e.g. Casey 2012; Casey et al. 2018).

At high- z such distortion is not observable, as only the long-wavelength part of the SED spectra is currently accessible with

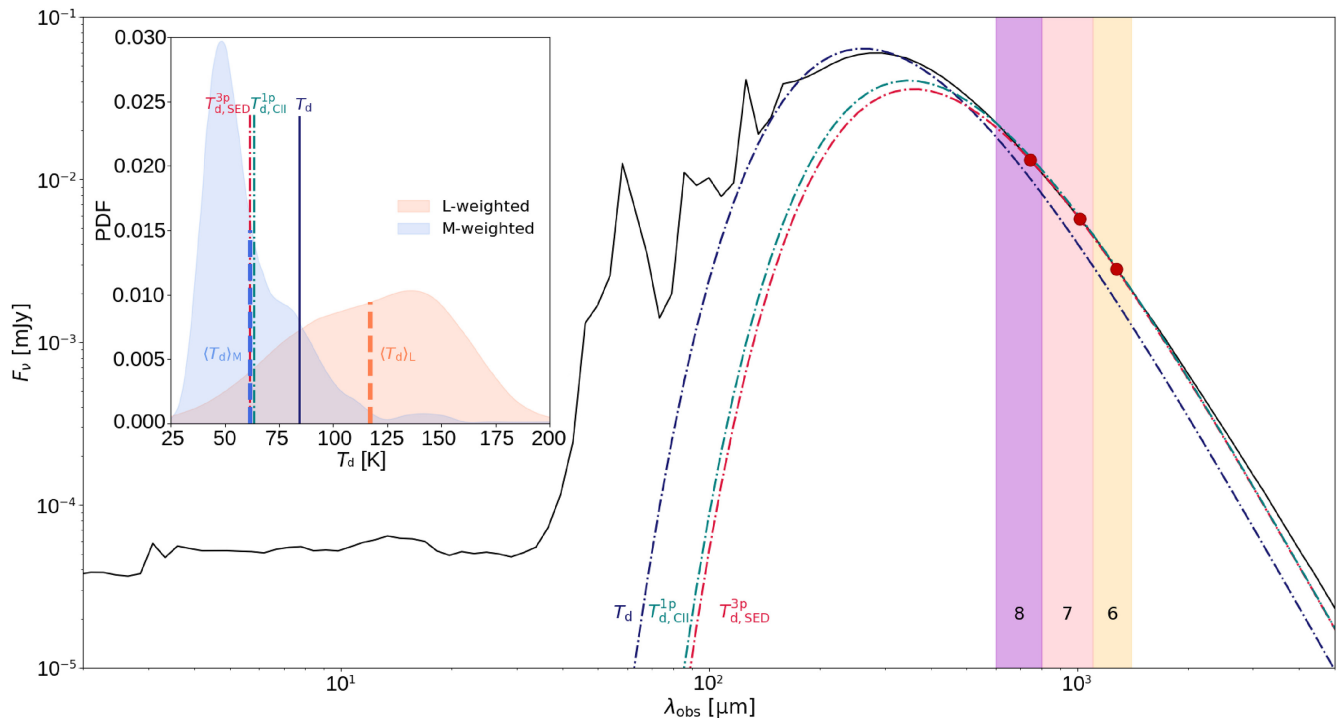


Figure A1. SED for the simulated galaxy Zinnia (serra05:s46:h0643, black solid line) extracted from the SERRA simulation suite. The dot-dashed lines show the curves obtained through a single-temperature grey-body fitting of the SED, with the two following methods: (a) a canonical SED fitting performed considering the three red ‘data points’ in ALMA bands 6, 7, and 8 (red line, $T_{d,SED}^{3p}$); (b) same as (a) but considering the full (i.e. MIR and FIR) galaxy SED (blue line, T_d); (c) the method presented in this work; it uses a single continuum observation and the [C II] emission (green line, $T_{d,CII}^{1p}$). The shaded regions mark the ALMA bands 6–8. *Subplot:* Comparison among the above dust temperatures values, the luminosity- (orange), and mass-weighted (blue) dust temperature PDFs derived for Zinnia. The PDFs mean values ($\langle T_d \rangle_L$ and $\langle T_d \rangle_M$) are indicated by dashed lines. See text for a detailed discussion.

ALMA (bands 6, 7, and 8). However, locally, where the whole SED is well sampled, it has been observed and studied by e.g. Casey (2012) within $z \sim 0$ submillimetre galaxies. In light of these considerations, the most appropriate and clean choice when comparing theoretical results with observations is to perform a single-temperature grey-body fit to the simulated SEDs in order to consistently obtain $T_{d,SED}$. In Fig. A1, we show the result of applying this procedure to the SED of the simulated $z \sim 6.7$ galaxy Zinnia (a.k.a. serra05:s46:h0643) from the SERRA simulation suite.

Full details on SERRA simulations are given in Pallottini (in preparation) and can be summarized as follows. Simulations zoom in on the evolution of $M_\star \sim 10^{10} M_\odot$ galaxies from $z = 100$ to $z = 6$ with a mass (spatial) resolution of the order of $10^4 M_\odot$ (30 pc at $z = 6$).²² [C II] emission is obtained by post-processing using grids of CLOUDY (Ferland et al. 2017) models accounting for the internal structure of molecular clouds (Vallini et al. 2017; Pallottini et al. 2019). Additionally, SKIRT (Baes & Camps 2015; Camps & Baes 2015) is used to obtain UV and dust continuum emission, with a setup similar to Behrens et al. (2018).

The main properties of Zinnia are summarized in Table A1. We proceed to compute and compare the following temperatures:

- (i) T_d : dust temperature obtained from fitting the full (i.e. MIR and FIR) galaxy SED with a single-T greybody.
- (ii) $T_{d,SED}^{3p}$: dust temperature obtained from fitting the galaxy SED at the frequencies corresponding to ALMA bands 6, 7, and 8 with a single-T greybody.
- (iii) $T_{d,CII}^{1p}$: dust temperature obtained with our method combining a single continuum data at 1900 GHz (rest frame) with the [C II] line emission data, as described in Section 4.
- (iv) $\langle T_d \rangle_M$: M-weighted dust temperature.
- (v) $\langle T_d \rangle_L$: L-weighted dust temperature.

We underline that in all these computations, as in the rest of the paper, we keep the dust emissivity index fixed to $\beta_d = 2.0$. Such an assumption is reasonable as this is close to the emissivity index retrieved from the simulation ($\beta_d = 1.7$ – 2 ; see Behrens et al. 2018 for the radiative transfer details). Hence, the free parameters in the fitting procedure are the dust temperature and dust mass ($40 \text{ K} \leq T_d \leq 200 \text{ K}$, and $10^3 M_\odot \leq M_d \leq 10^7 M_\odot$).

All these temperatures are compared in the subplot in the upper left corner of Fig. A1 and the derived properties are summarized in Table A2. Our method gives a dust temperature value $T_{d,CII}^{1p} = 63.4 \pm 0.5 \text{ K}$, consistent with the result that one obtains with the usual SED fitting technique using three points corresponding to the available ALMA bands at this redshift, $T_{d,SED}^{3p} = 62 \pm 2 \text{ K}$. For this galaxy, the value of $T_{d,SED}^{3p} \sim T_{d,CII}^{1p}$ is also consistent with the M-weighted temperature, $\langle T_d \rangle_M = 61 \text{ K}$. Instead both $\langle T_d \rangle_L = 117 \text{ K}$ and $T_d = 84 \text{ K}$ are larger than the previous values as they are more sensitive to the small amount of dust with physical temperatures up to 150 K (see the L-weighted PDF in the subplot of Fig. A1).

²²The simulation adopts a multigroup radiative transfer version of the hydrodynamical code RAMSES (Rosdahl et al. 2013; Teyssier et al. 2013) that includes thermochemical evolution via KROME (Grassi et al. 2014; see Bovino et al. 2014; Pallottini et al. 2017b, for the network and included processes), which is coupled to the evolution of radiation (Pallottini et al. 2019; Decataldo et al. 2020). Stellar feedback includes SN explosions, OB/AGB winds, and both in the thermal and turbulent form (see Pallottini et al. 2017a, for details).

Table A1. Properties of our high- z simulated galaxy Zinnia (a.k.a. serra05:s46:h0643). We note that the parameter $y = r_{\text{C II}}/r_{\star} = 1.0$ is selected by definition, i.e. we only consider the emission coming from the central ~ 1.5 kpc region.

Galaxy	z	F_{ν_0} (μJy)	Z (Z_{\odot})	$\log \Sigma_{\text{SFR}}$ ($\text{M}_{\odot} \text{ yr}^{-1} \text{ kpc}^{-2}$)	$L_{\text{C II}}$ ($10^8 L_{\odot}$)	κ_s	$y = r_{\text{C II}}/r_{\star}$	M_{\star} (10^9 M_{\odot})
Zinnia	6.6847	2.81	0.07	2.56	2.05	4.29	1.00*	2.19

Table A2. Comparison between the properties predicted with our method ('this work'), and derived through a single-temperature grey-body fitting of the simulated flux in ALMA bands 6, 7, and 8 of galaxy serra05:s46:h0643. In the SED fitting procedure, we keep the dust emissivity index fixed at $\beta = 2.0$, as in our analytical method, and consider a 1 per cent uncertainty on all the galaxy properties derived from the simulation and listed in Table A1. We underline that our predictions correspond to $T_{\text{d,C II}}$.

Galaxy	$\alpha_{\text{C II, Hz}}$	$T_{\text{d,SED}}$ (K)	M_{d} (10^5 M_{\odot})	y_{d} ($10^{-3} \text{ M}_{\odot}/\text{SN}$)
serra0643	8.9	62 ± 2	2.0 ± 0.8	–
This work	8.76 ± 0.07	63.4 ± 0.5	1.94 ± 0.03	4.67 ± 0.06

This comparison shows that the single-T approximation often used might lead to a misinterpretation of the physical properties of the galaxy depending directly on T_{d} . Moreover, whenever theoretical studies and observations are compared, it is necessary to pay particular attention to the definition of the dust temperature used and to the fitting procedure. We suggest that a uniform, meaningful

comparison is best performed using either $T_{\text{d,SED}}^{3p}$ or, as we propose here, $T_{\text{d,C II}}^{1p}$, when only a single measurement is available. It is very reassuring that the two procedures yield essentially the same result. These quantities can be also easily derived from the simulated spectrum, and readily compared with data.

APPENDIX B: FULL SED FITTING OF THE LOCAL SAMPLE

We also performed a grey-body fit on the available IR continuum data for the sources in our local sample (see Section 3 for the sources details). The result is shown here in Fig. B1. In all cases, we find dust temperatures that are consistent (within errors) with those obtained from the continuum fluxes ratio reported in Table 1. It is worth mentioning that in 22 per cent of the cases (4 out of 19) not more than two continuum data are available in the literature. For this reason, we prefer to use the continuum fluxes ratio method for the estimation of $T_{\text{d,SED}}$ in the main text. Anyhow, changing to SED fitting does not affect our conclusions on the validity of method.

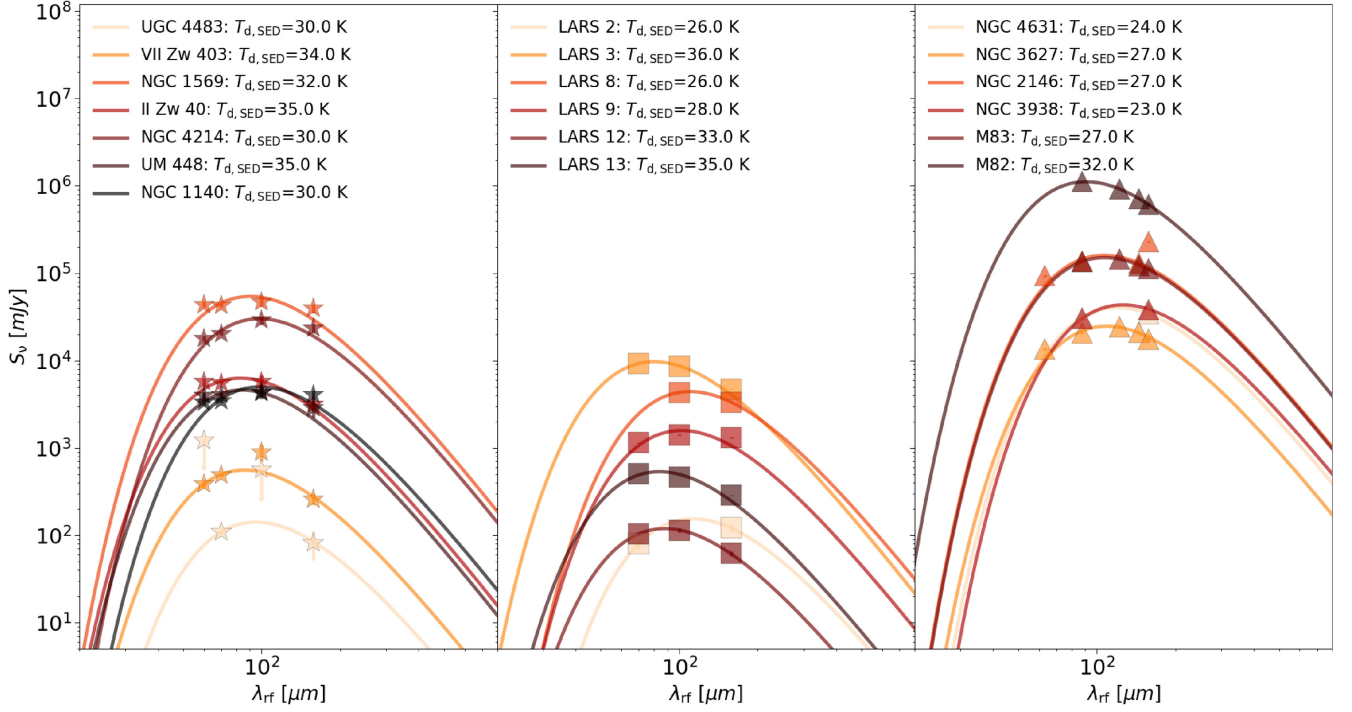


Figure B1. FIR SED grey-body fit ($\beta_d = 2.0$) for the galaxies in the local sample. From left to right: DL subsample (Nilson 1973; Engelbracht et al. 2008; DL; Cormier et al. 2019, ID 0-6 in the paper), LARS subsample (Puschig et al. 2020, ID 7-12), and PACS data base subsample (Jarrett et al. 2003; Caldú-Primo & Cruz-González 2008; Leroy et al. 2008; Groves et al. 2015; Fernandez-Ontiveros et al. 2016, ID 13-18). In all cases, we find consistent temperatures (within the errors) with the ones obtained through continuum fluxes ratio in the paper (See Table 1).

This paper has been typeset from a \LaTeX file prepared by the author.